Physical modelling on gas migration behavior and its impact on seabed stability

S.L. Wang, Y. Chen, Y.W. Long, D.Q. Kong, B. Zhu
Institute of Hypergravity Science and Technology, Zhejiang University, Hangzhou, China
College of Civil Engineering and Architecture, Zhejiang University, Hangzhou, China, binzhu@zju.edu.cn (Corr. Author)

ABSTRACT: Significant amounts of free gas exist within marine clay sediments. An in-depth investigation into the mechanisms of gas trapping, migration, and their impact on seabed stability is crucial for enhancing the service performance of marine geotechnical engineering facilities. In this study, a physical modelling apparatus to simulate gas migration in submarine soft clay was developed, which primarily comprised a dual-cylinder plunger pump capable of long-duration, high-precision gas injection (flow rate range: 0.0001-100 mL/min, accuracy: 0.0001 mL/min) and a model box. The model seabed was prepared using Malaysian kaolin clay. Gas injection tests were conducted at a constant flow rate (10 mL/min) on two model seabeds with different strengths. Pore pressure transducers and volumetric water content sensors were employed to monitor real-time pore pressure responses and gas distribution changes within the seabed. The critical pressure for gas invasion, the rise velocity of gas bubbles, and the spatial distribution characteristics of pore pressure induced by gas migration were monitored, and the long-term existence of a stable gas cavity was observed. Moreover, the potential gas-induced evolution of seabed surface features, such as domes and pockmarks following gas eruptions, was explored. These findings facilitate our understanding of gas behaviour in marine clay and associated engineering hazard mechanisms.

1 INTRODUCTION

Shallow gas, predominantly methane of either biogenic or thermogenic origin, is widely distributed in continental margin sediments (Floodgate & Judd, 1992). Its presence and migration are not only a key component of the global carbon cycle, but also a significant trigger for submarine geohazards. Gas accumulation and upward migration through sediments can significantly undermine seabed soil strength and stability, potentially initiating hazards such as submarine landslides (Ma et al., 2021). Furthermore, gas eruptions may damage submarine pipelines, cables, and other engineering infrastructures (Duan et al., 2023) while simultaneously driving the formation of seabed morphologies such as pockmarks and mud volcanoes (Sun et al., 2012). Therefore, investigating the occurrence modes and migration processes of shallow gas, along with their interactions with the seabed, is crucial for assessing submarine geotechnical risks and understanding seabed geomorphological evolution.

Given the technical challenges, high costs associated with in-situ observations, and the inherent complexity of natural seabed environments, experimental investigations have become indispensable for elucidating gas migration and associated hazard formation mechanisms. For sandy sediments, Nermoen et al. (2010) utilized glass beads to quantify the critical gas pressure and flow velocity for fluidization under varying seabed thicknesses and injection port widths, and developed a theoretical model. Mourgues et al. (2012) demonstrated that imposed pore fluid overpressure in diatomite models can promote the formation of conical fractures through a mechanism of elastic stress rotation. Varas et al. (2015), experimenting with saturated glass beads, observed parabolic fluidized zones and dynamic processes of bubbling, degassing, and flow-to-fracture transition.

For clayey sediment, Nian et al. (2022) used South China Sea samples for gas injection experiments and identified both shear and tensile failure modes in gas-induced submarine landslides. Zhu et al. (2023) employed cohesive transparent soil to model landslides triggered by hydrate dissociation, and visualized the development of lateral and vertical gas migration paths and subsequent progressive slope failure. Through quasi-2D experiments, Vaknin et al. (2024) explored bubble migration, eruption, and pockmark formation in kaolin seabeds of varying thickness and strength, proposing three distinct failure modes. Pimentel et al. (2025) conducted experiments on silty slopes and identified the formation of mounds, pockmarks, and fractures during gas migration.

Current research on gas-induced failure mechanisms is relatively well-established. However, further experimental studies are still required regarding issues such as how gas selects preferential pathways in clayey seabeds and how its migration process affects the seabed's pore pressure field. This study presents two laboratory model tests on kaolin model seabeds with different strength profiles. A high-precision dual-cylinder plunger pump was used to inject gas at a constant flow rate. The spatial distributions of gas and associated pore pressure responses were monitored in real-time with volumetric water content sensors and pore pressure transducers, respectively. This study focuses on the dynamic migration process and the influence of seabed properties (such as strength, water content, and density) on gas migration pathways, as well as the formation of characteristic surface features during gas accumulation and venting. This research is expected to provide experimental insights into the mechanisms of shallow gas geohazards in submarine environments.

2 METHODS

2.1 Experimental setup

The experimental setup is illustrated in Figure 1. A model box with internal dimensions of 55 cm × 28 cm × 48 cm (length × width × height) was used. A gas injection pipe with a diameter of 5 mm and a length of 10 cm was fixed at the center of the bottom. Three volumetric water content sensors (VWCSs) were installed above the gas injection port. Each sensor measures the average volumetric water content θ within a specific soil volume V, which equals 240 mL in terms of the sensor in this study, as delineated by the white areas in Figures 1(a) and 1(b).

To calibrate the volumetric water content sensors, Malaysian kaolin clay samples were prepared at gravimetric water contents of 0%, 20%, 40%, 60%, 80%, and 100%. Each sample was compacted in layers to a fixed volume of 250 mL. The sensors were then fully inserted, and the output voltages U were recorded. Subsequently, the actual gravimetric water content w and dry density ρ_d of each sample were measured, allowing the volumetric water content θ to be calculated as $\theta = w\rho_d/\rho_w$. This established the calibration relationship between U and θ.

The gas volume V_a within the sensor's measurement range is estimated using the equation $V_a = V\text{-}V_w\text{-}V_s = V\text{-}\theta V\text{-}\theta V/\omega G_s$, where V_w is the water volume, V_s is the soil particle volume, ω is the gravimetric water content of the soil matrix, and G_s is the specific gravity of the soil solids. In the gas injection experiment, the gas phase predominantly exists as discrete bubbles or connected pathways, which differs from the uniformly distributed gas condition assumed during sensor calibration. This discrepancy may introduce minor quantitative deviations in the absolute gas volume estimation. Nevertheless, the approach remains valid for capturing the relative spatial distribution and dynamic evolution of gas within the seabed. Additionally, pore pressure transducers (PPTs) were installed both near the injection port and in the far-field region of the seabed to monitor the pore pressure response during gas migration.

Gas was injected into the model seabed at a constant flow rate using a dual-cylinder plunger pump, as shown in Figure 1(c). This pump operates in a dual-cylinder series mode, with the two pumps injecting gas alternately to ensure a continuous and stable flow over extended periods. It offers a flow rate range of 0.0001 to 100 mL/min with an accuracy of ±0.0001 mL/min. The injection pressure is monitored by built-in pressure sensors, which have a range of 0–200 kPa and an accuracy of ±0.01 kPa.

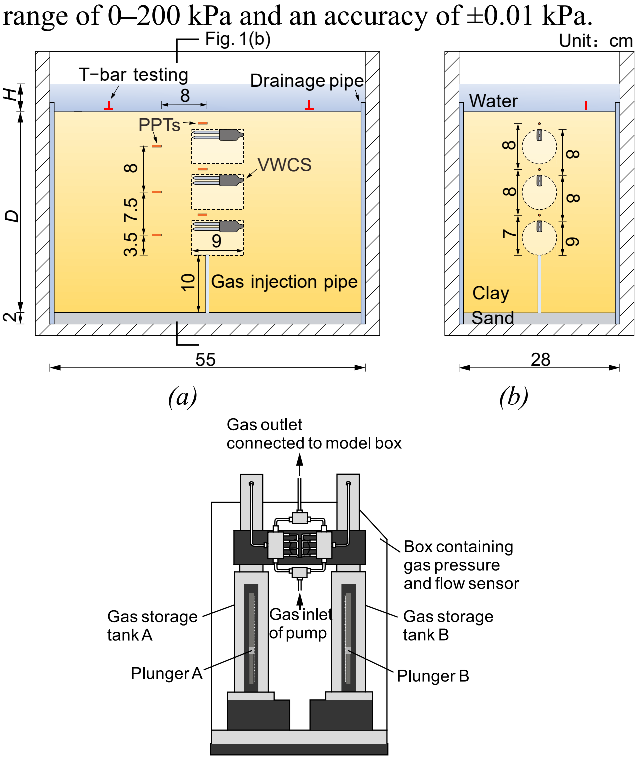

(c)

Figure 1 Experimental setup: (a) front view of model box; (b) side view of model box; (c) dual-cylinder plunger pump

2.2 Experimental procedure

The model seabed was prepared using Malaysian kaolin clay, with a measured plastic limit (PL) of 35%, liquid limit (LL) of 80%, and plastic index (PI) of 45 (Goh 2003). Kaolin powder was mixed with water to prepare a slurry with a water content of 160% (twice its LL). This slurry was then poured into the model tank, which had a pre-installed 2cm thick drainage sand layer at the bottom. Drainage pipes fixed at the four corners of the model box facilitated two-way drainage during consolidation. A total of two model seabeds were prepared with different consolidation histories: Seabed 1 was consolidated under a surcharge load for 7 days. After load removal, a small amount of additional slurry was added to level the surface, and the seabed was left to stand for another 5 days. The final soil height was 35 cm. Seabed 2 was consolidated under self-weight for 33 days, resulting in a final seabed height of 36cm. These two distinct consolidation methods were chosen to generate seabeds with contrasting strength profiles: Seabed 1 was expected to exhibit relatively uniform shear strength with depth, while Seabed 2 was anticipated to develop a strength profile increasing approximately linearly with depth. This experimental design enables a comparative investigation of gas migration behavior in seabeds characterized by different strength distributions. Following consolidation, the gas injection pipe was connected to the plunger pump. Gas was injected into the seabed at a constant rate of 10 mL/min. After gas injection, the seabed strength profile was measured using a T-bar penetrometer, and the saturated density and gravimetric water content of the seabed were measured through layered sampling.

3 RESULTS AND DISCUSSION

3.1 Results of Test 1

3.1.1 Seabed properties

Figure 2 shows the strength, density, and water content profiles of Seabed 1. As shown in Figure 2(a), the overall seabed strength is low, generally not exceeding 3.5 kPa. Within the upper 13 cm, the seabed strength is comparable between the left (Point L) and right (Point R) sides. Below this depth, the left side of the seabed exhibits slightly lower strength compared to the right, with a sharp strength increase observed between 13 cm and 15 cm.

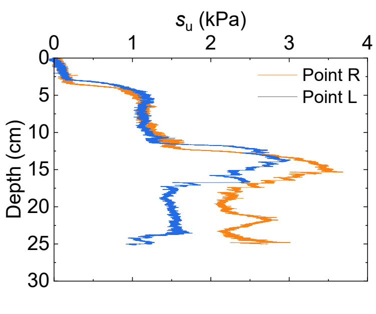

(a)

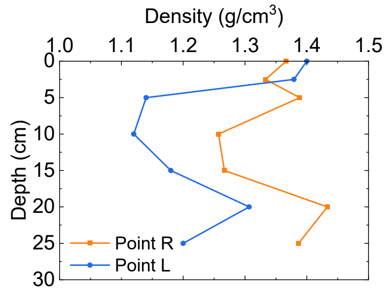

(b)

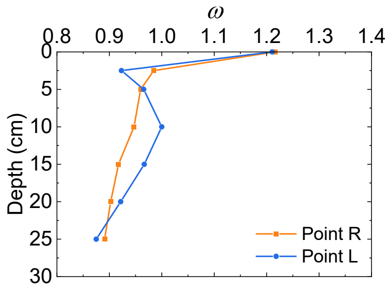

(c)

Figure 2 Soil properties of Seabed 1: (a) undrained shear strength; (b) saturated density; (c) gravimetric water content

The seabed density typically ranges from 1.1 to 1.4 g/cm^3, with the left side being generally less dense than the right (Figure 2b). The water content decreases with depth, reaching a minimum of approximately 90%, and is generally higher on the left side than on the right (Figure 2c).

3.1.2 Gas migration process

Figures 3(a)-(c) show the temporal variations in gas pressure, volume, and seabed pore water pressure during gas migration in Seabed 1, respectively. The entire gas injection process lasted about 52 minutes. Although pore pressure sensor data were lost after 35 minutes due to data storage issues, the recorded data successfully captured the primary stages of gas migration. Based on the observed gas behavior, the migration process can be divided into four distinct stages.

Stage I: Gas accumulation. During this stage, the gas pressure is insufficient to overcome the overburden pressure and soil strength. Consequently, gas accumulates within the injection pipe, leading to a continuous pressure increase (Figure 3a).

Stage II: In-situ bubble growth. Once the gas pressure reaches a critical invasion threshold P_{cr} of approximately 13.83 kPa, gas begins to enter the soil, accompanied by a significant pressure drop (Figure 3a). Considering the total overburden pressure above the gas injection pipe, $P_0 = 3.33$ kPa, and the average undrained shear strength of soil at that depth, s_{u_inj} = 1.91 kPa, the net invasion pressure-to-strength ratio, defined as $(P_{cr}$-$P_0)/s_{u\_inj}$, is calculated to be 5.50.

About one minute later, the nearest (PPT1, PPT4) and the farthest (PPT6) pore pressure transducers register a response (Figure 3c), while other PPTs show no discernible change. This differential response is likely attributable to the shading effect of VWCSs, where the presence of the sensors may have locally influenced pore pressure propagation. The volumetric water content sensors (VWCS) show no change (Figure 3b), which suggests that the gas had not yet begun to migrate upward but is likely accumulating near the injection port to form a growing bubble.

Stage III: Cyclic bubble growth and migration. At around 10 minutes, the gas pressure decreases slightly (Figure 3a). Concurrently, VWCS2 records a sharp increase followed by an immediate decrease (Figure 3b), indicating the detachment and upward migration of the first bubble from the injection port. The bubble's ascent velocity is estimated at 2.34 cm/s, calculated from the time difference between the increase in data of VWCS2 and the bubble's observed release at the seabed surface. This estimation assumes a linear migration path and constant rise velocity between VWCS2 and the surface. Subsequently, both gas pressure and bubble volume exhibit periodic fluctuations, indicating repeated cycles of bubble formation and release (Figures 3a, b). The pore pressure drops significantly about one minute after the first bubble escapes, followed by oscillatory changes (Figure 3c).

Stage IV: Stable gas cavity formation. At approximately 30 minutes, the reading from VWCS2 suddenly increases and stabilizes around 30 mL (Figure 3b). This is attributed to the formation of a stable gas cavity, likely because the higher soil strength near VWCS2 (Figure 2a) impedes further upward migration, trapping the gas beneath this zone.

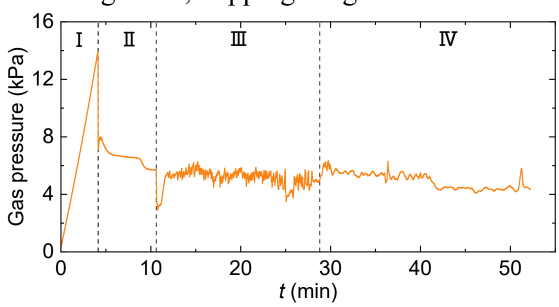

(a)

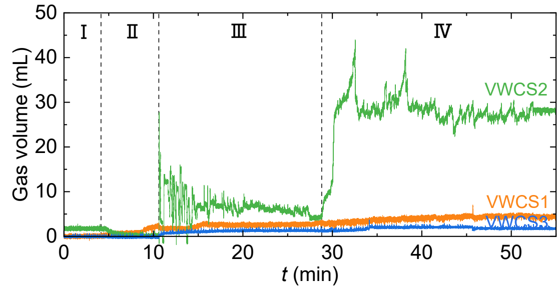

(b)

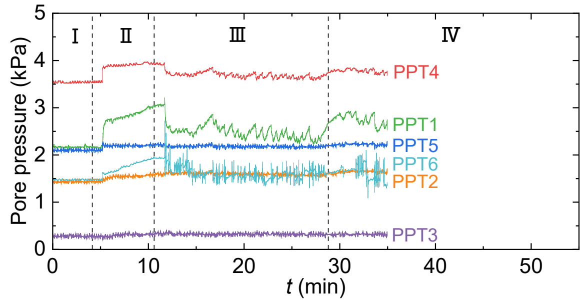

(c)

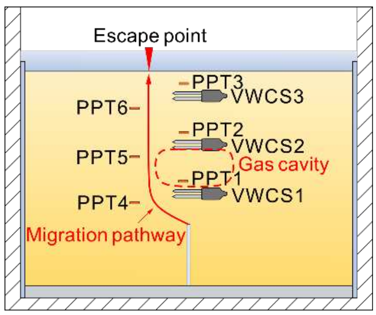

(d)

Figure 3 Gas migration process in Seabed 1: (a) time trace of gas pressure at injection port; (b) time trace of gas volume; (c) time trace of pore pressure; (d) schematic diagram of migration process

Synthesizing the data from the pressure and water content sensors, it can be inferred that in Seabed 1, gas escapes from the left side of the injection port, bypasses VWCS1, and ultimately accumulates between VWCS1 and VWCS2 (Figure 3d). This migration pathway is attributed to the lower soil strength on the left side, which provides a preferential route for gas movement.

3.1.3 Seabed surface feature

Figure 4 shows the morphological changes of the seabed surface. The initial growth of the first bubble within the seabed induces significant deformation, manifesting as a surface dome (Figure 4a).

(a) (b)

Figure 4 Seabed surface features in Seabed 1: (a) side view before first bubble escapes; (b) top view after bubbles' periodic escape

The eruption of the bubble causes substantial disturbance to the seabed and carries a small amount of soil to the surface. After multiple eruption cycles, a disturbed zone with a diameter of approximately 5 cm (equivalent to 10 times the injection port diameter) formed on the seabed surface (Figure 4b). The center of this zone contained large soil fragments, while the periphery is characterized by finer, dispersed particles that are carried out and subsequently settle.

3.2 Results of Test 2

3.2.1 Seabed properties

The geotechnical properties of Seabed 2 are summarized in Figure 5. As T-bar data for the left side are unavailable, only the strength profile on the right side of the gas injection pipe is presented. Overall, Seabed 2 exhibits lower strength than Seabed 1. The strength increases almost linearly with depth, reaching a maximum of approximately 1.5 kPa (Figure 5a). The density range is similar to that of Seabed 1 (1.1–1.4 g/cm³), with the left side being generally less dense (Figure 5b). The water content decreases with depth and was approximately 10% higher on average than in Seabed 1, with a minimum value of about 105%. The water content on both sides of the seabed is basically consistent (Figure 5c).

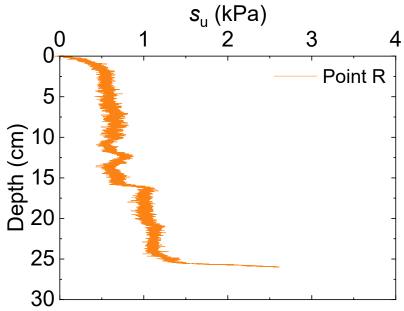

(a)

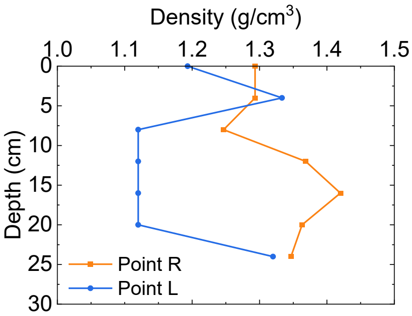

(b)

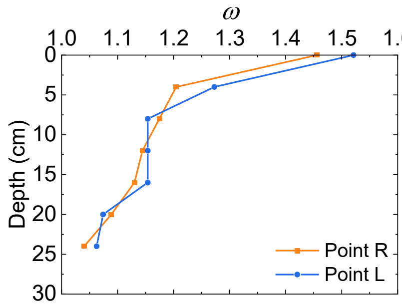

(c)

Figure 5 Soil properties of Seabed 2: (a) undrained shear strength; (b) saturated density; (c) gravimetric water content

3.2.2 Gas migration process

The temporal evolutions of gas pressure, volume, and pore water pressure during gas migration in Seabed 2 are depicted in Figures 6(a)-(c). The total injection duration is approximately 65 minutes, and the process can be categorized into three main stages.

Stage I: Gas accumulation. This stage is consistent with the behavior observed in Seabed 1, characterized by continuous gas accumulation in the injection pipe and a rise in pressure (Figure 6a).

Stage II: In-situ bubble growth. Upon reaching a critical invasion pressure P_{cr} of 15.41 kPa, the gas invades into the soil, resulting in a significant pressure drop followed by stabilization around 6 kPa (Figure 6a). The total overburden above the injection pipe P_0 and the undrained shear strength of soil at that depth s_{u_inj} are estimated to be 3.36 kPa and 2.59 kPa, respectively. This yields a net invasion pressure-to-strength ratio of $(P_{cr}\text{-}P_0)/s_{u\_inj} = 4.65$. The continuous increase in gas volume recorded by VWCS1 (Figure 6b) directly above the injection port indicates the formation and growth of a bubble at that location. The moment of gas invasion triggers an immediate, sharp response in PPT4, located on the upper left of the injection port. PPT1 (directly above the port) and the more distant PPT5 and PPT2 exhibit a delayed response (Figure 6c), registering changes about 3 minutes after the initial invasion. This delay pattern can also be attributed to the shading effect caused by sensor placement.

Stage III: Cyclic bubble growth and migration. This stage is marked by three sharp declines in gas volume (at approximately 13, 33, and 43 minutes, Figure 6b), signaling massive and rapid gas release events where accumulated gas escapes, with virtually no gas remaining stable after 43 minutes. Between these events, the gas volume showed periodic fluctuations, reflecting smaller-scale accumulation and release cycles. The gas pressure exhibits a slight increase after the 43-minute release, followed by minor periodic fluctuations (Figure 6a). The pore pressure at PPT1, directly above the injection port, decreases correspondingly during the three major gas release events, while other transducers record no significant changes (Figure 6c).

The gas migration pathway in Seabed 2 is generally similar to that in Seabed 1, favoring the left side. However, the initial path in Seabed 2 proceeds upward near the centerline before deflecting to the left after passing VWCS1 and PPT1 (Figure 6d). This deviation suggests that the physical presence of the sensors may have obstructed the primary migration path, diverting the gas towards the sensor-free left side. Such interference highlights an inherent limitation of the experimental setup. In real seabed environments, however, analogous obstructions such as boulders, sediment heterogeneities, or engineered structures can similarly influence gas migration routes. Therefore, the key finding that gas preferentially migrates through zones of lower strength and avoids rigid obstacles remains geotechnically meaningful and offers useful insight for predicting gas migration behavior in heterogeneous seabed conditions.

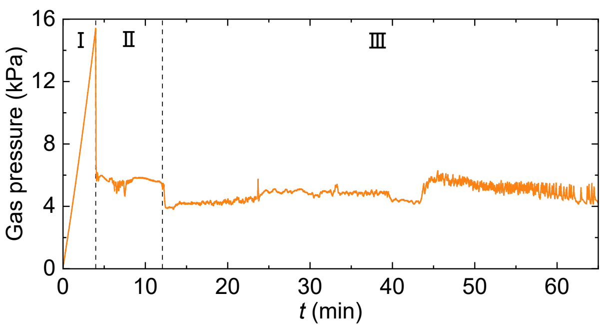

(a)

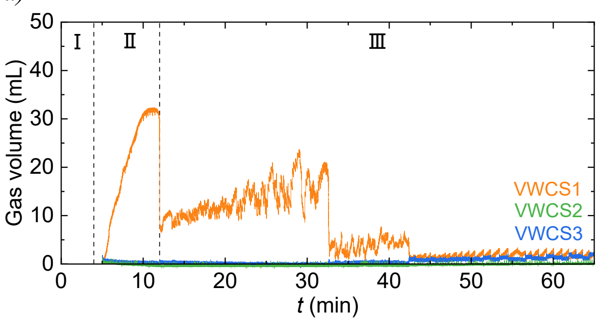

(b)

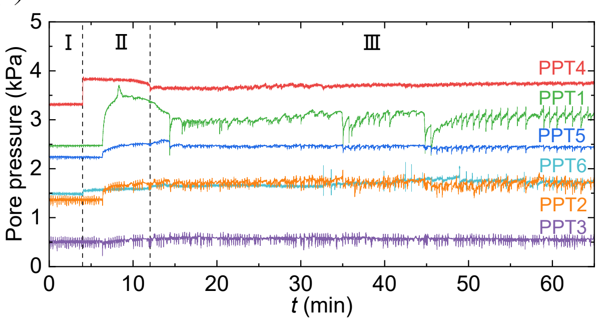

(c)

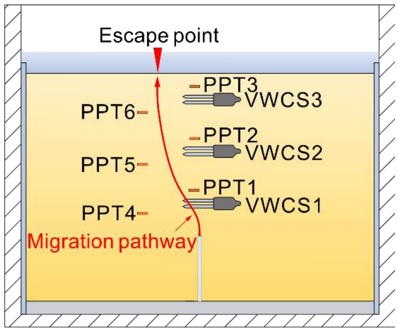

(d)

Figure 6 Gas migration process in Seabed 2: (a) time trace of gas pressure at injection port; (b) time trace of gas volume; (c) time trace of pore pressure; (d) schematic diagram of migration process

3.2.3 Seabed surface feature

Similar to Seabed 1, gas accumulation causes substantial seabed deformation and surface uplift (Figure 7a). The magnitude of uplift is greater than in Test 1, indicating the formation of a larger initial bubble in Seabed 2. Following multiple gas eruptions, a pockmark depression with a diameter of approximately 8 cm (16 times the injection port diameter) forms near the eruption point, containing a small amount of soil fragments at its center (Figure 7b, c). The pockmark likely resulted from the collapse of the gas cavity after the escape of a large gas volume.

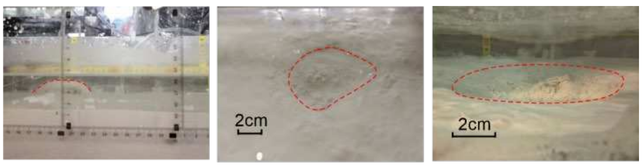

(a) (b) (c)

Fig.7 Seabed surface features in Seabed 2: (a) side view before first bubble escapes; (b) top view after bubbles' periodic escape; (c) side view after bubbles' periodic escape

These observations demonstrate that even in seabeds with very low undrained shear strength (< 4 kPa), gas migration can trigger the formation of distinct geohazards, such as domes and pockmarks. Such seabed features pose direct risks to marine infrastructures, including subsea pipelines and foundations, by potentially causing localized subsidence, loss of support, or impact loading during eruption events. Therefore, detailed site characterization, particularly regarding shallow gas occurrence, is essential prior to engineering development in gas-prone regions. Moreover, the presence of submarine domes may serve as a surface indicator of significant gas accumulations at depth, offering valuable insight for hazard footprint estimation and early-stage geohazard assessment.

4 CONCLUSIONS

This study developed an experimental apparatus to simulate gas migration in clayey seabeds under constant-flow injection. By employing volumetric water content sensors and pore pressure transducers, the spatiotemporal evolution of gas and the corresponding pore pressure responses were successfully monitored in real time. Two gas injection tests reveal that the migration process can be divided into three primary stages: (I) gas accumulation, (II) in-situ bubble growth, and (III) cyclic bubble growth and migration. An additional stage of (IV) stable gas cavity formation is identified in Seabed 1.

The spatial distribution of seabed strength is decisive to gas migration pathways and their eventual occurrence state. Gas consistently favors pathways through zones of lower strength and density. In Seabed 1, which exhibits higher and more heterogeneous strength, gas accumulated beneath a localized high-strength zone to form a stable cavity. Seabed 2, with its lower and more uniform strength profile, is dominated by cyclic episodes of gas accumulation and escape, preventing the long-term stabilization of gas within the soil.

The accumulation and subsequent eruption of gas induce significant seabed deformation. Prior to eruption, the primary surface manifestation is the formation of domes. Post-eruption, disturbed zones form on the seabed surface, with diameters exceeding 10 times that of the injection port. The sudden escape of a large gas volume led to sediment collapse, resulting in the formation of a pockmark.

It is important to note that the sensors used in this study may have influenced the gas migration process, potentially diverting the original pathways. Future work should therefore explore non-intrusive monitoring techniques, such as computed tomography (CT). Additionally, these experiments were conducted under a normal gravitational field (1g) and do not replicate the in-situ stress conditions of a marine environment. Consequently, the absolute values of stress and overburden pressure reported herein cannot be directly extrapolated to field-scale predictions. Nevertheless, the qualitative observations, such as the staged migration process, preferential pathways toward weaker zones, and surface feature formation, provide insights that are likely scale-independent. Moreover, the normalized net invasion pressure-to-strength ratios offer a dimensionless basis for preliminary comparisons with field conditions. Centrifuge modeling is recommended for future research to investigate gas migration mechanisms under representative stress levels and over longer durations.

ACKNOWLEDGEMENTS

The authors are grateful for the financial support provided by the National Natural Science Foundation of China (Grant No. 52588202, 52571309, 52127815).

REFERENCES

Duan, X., Yin, P., Tsona, N., Cao, K., Xie, Y., He, X., ... & Lv, S. 2023. Biogenic methane in coastal unconsoli dated sediment systems: A review. *Environmental Res earch*, 227, 115803. https://doi.org/10.1016/j.envres.2 023.115803

Floodgate, G. D., & Judd, A. G. (1992). The origins of shallow gas. *Continental Shelf Research*, 12(10), 1145-1156. https://doi.org/10.1016/0278-4343(92)90075-U

Goh, T.L., 2003. *Stabilisation of an excavation by an embedded improved soil layer*. Ph.D. Thesis, National University of Singapore.

Ma, G., Zhan, L., Lu, H. & Hou, G., 2021. Structures in shallow marine sediments associated with gas and fluid migration. *Journal of Marine Science and Engineering*, 9(4), 396. https://doi.org/10.3390/jmse9040396

Mourgues, R., Bureau, D., Bodet, L., Gay, A., & Gressier, J. B. (2012). Formation of conical fractures in sedimentary basins: Experiments involving pore fluids and implications for sandstone intrusion mechanisms. *Earth and Planetary Science Letters*, 313, 67-78. https://doi.org/10.1016/j.epsl.2011.10.029

Nermoen, A., Galland, O., Jettestuen, E., Fristad, K., Podl adchikov, Y., Svensen, H., & Malthe-Sørenssen, A. (2 010). Experimental and analytic modeling of pierceme nt structures. *Journal of Geophysical Research: Solid Earth*, 115(B10). https://doi.org/10.1029/2010JB0075 83

Nian T K, Song X L, Zhao W, Jiao H B, Guo X S. 2022. Submarine slope failure due to overpressure fluid asso ciated with gas hydrate dissociation. *Environmental G eotechnics*, 9(2): 108-123. https://doi.org/10.1680/jen ge.19.00070

Pimentel, G. L., Puhl, E., da Silva, D. B., de Azevedo, K. S., Schenk, C. V., da Silva, F. R. S., ... & Ketzer, M. (2025). Sediment deformation and structures formed b y gas migration and seafloor exudation: An experimen tal approach. *Marine Geology*, 484, 107501. https://do i.org/10.1016/j.margeo.2025.107501

Sun, Q., Wu, S., Cartwright, J., & Dong, D. 2012. Shallo w gas and focused fluid flow systems in the Pearl Rive r Mouth Basin, northern South China Sea. *Marine Geo logy*, 315, 1-14. https://doi.org/10.1016/j.margeo.2012. 05.003

Vaknin, I., Aharonov, E., Holtzman, R., & Katz, O. 2024. Gas seepage and pockmark formation from subsurfac e reservoirs: Insights from table-top experiments. *Jour* *nal of Geophysical Research: Solid Earth*, 129(4), e2023JB028255. https://doi.org/10.1029/2023JB028255

Varas, G., Ramos, G., Géminard, J. C., & Vidal, V. (2015). Flow and fracture in water-saturated, unconstrained granular beds. *Frontiers in Physics*, 3, 44. https://doi.org/10.3389/fphy.2015.00044

Zhu, C., Jiao, X., Cheng, S., Li, Q., Liu, K., Shan, H., ... & Jia, Y. (2023). Visualising fluid migration due to hydrate dissociation: implications for submarine slides. *Environmental Geotechnics*, 10(3), 218-226. https://doi.org/10.1680/jenge.19.00068